Two Foreshock Sequences Post Gulia and Wiemer (2019)

Kelian Dascher-Cousineau*[1], Thorne Lay[1], and Emily E. Brodsky[1]

Abstract

Recognizing earthquakes as foreshocks in real time would provide a valuable forecasting capability. In a recent study, Gulia and Wiemer (2019) proposed a traffic-light system that relies on abrupt changes in *b*-values relative to background values. The approach utilizes high-resolution earthquake catalogs to monitor localized regions around the largest events and distinguish foreshock sequences (reduced *b*-values) from aftershock sequences (increased *b*-values). The recent well-recorded earthquake foreshock sequences in Ridgecrest, California, and Maria Antonia, Puerto Rico, provide an opportunity to test the procedure. For Ridgecrest, our *b*-value time series indicates an elevated risk of a larger impending earthquake during the M_w 6.4 foreshock sequence and provides an ambiguous identification of the onset of the M_w 7.1 aftershock sequence. However, the exact result depends strongly on expert judgment. Monte Carlo sampling across a range of reasonable decisions most often results in ambiguous warning levels. In the case of the Puerto Rico sequence, we record significant drops in *b*-value prior to and following the largest event (M_w 6.4) in the sequence. The *b*-value has still not returned to background levels (12 February 2020). The Ridgecrest sequence roughly conforms to expectations; the Puerto Rico sequence will only do so if a larger event occurs in the future with an ensuing *b*-value increase. Any real-time implementation of this approach will require dense instrumentation, consistent (versioned) low completeness catalogs, well-calibrated maps of regionalized background *b*-values, systematic real-time catalog production, and robust decision making about the event source volumes to analyze.

Cite this article as Dascher-Cousineau, K., T. Lay, and E. E. Brodsky (2020). Two Foreshock Sequences Post Gulia and Wiemer (2019), *Seismol. Res. Lett.* **91**, 2843–2850, doi: 10.1785/0220200082.

Introduction

Global statistical analyses of earthquake sequences and the advent of high-resolution earthquake catalogs demonstrate that foreshock sequences often precede large earthquakes (e.g., Bouchon *et al.*, 2013; Marsan *et al.*, 2014; Mignan, 2015; Seif *et al.*, 2019; Trugman and Ross, 2019). Recognizing that an event is a foreshock would provide useful forecasting capability. However, decades of work have failed to establish a robust feature of individual foreshocks that distinguishes them from mainshocks or their aftershocks. An alternative would be to find a distinct statistical attribute of a sequence of events that occurs prior to a mainshock versus a sequence of events that follows a mainshock (e.g., Helmstetter *et al.*, 2003). Foreshocks may be distinctive due to some precursory loading process or influence from the locked zone of the subsequent mainshock, neither of which will exist for the aftershock sequence (e.g., Brodsky and Lay, 2014). Recently, Gulia and Wiemer (2019) proposed that abrupt changes in magnitude–frequency distribution relative to background levels in localized regions around the largest events provide such a distinguishing attribute. They evaluated their method for 27 earthquake sequences not followed by a second mainshock, plus two followed by a second mainshock (Amatrice, Italy, and Kumamoto, Japan). Eighteen correct negatives, two true positives, 10 neutral alarms, counted neither as successes or failures, and one false alarm yielded a 95% success rate in discriminating foreshock sequences from aftershock sequences. Their approach relies on time-varying estimates of the slope of the cumulative magnitude–frequency distribution, or *b*-value of the Gutenberg–Richter relationship:

$$b = \frac{N}{\log(10)\sum_{i=1}^{N}(M_i - M_c + \Delta_M/2)}. \quad (1)$$

The *b*-value, here estimated by the maximum-likelihood method (Aki, 1965; Utsu, 1965), is calculated in a sliding time window, in which N is the number of events in the selected window of space and time, M_i is the magnitude of each event, M_c is the catalog completeness magnitude (lowest magnitude for which all events are thought to be detected), and $\Delta_M/2$ is

1. University of California, Santa Cruz, Department of Earth and Planetary Sciences, Santa Cruz, California, U.S.A.

*Corresponding author: kdascher@ucsc.edu

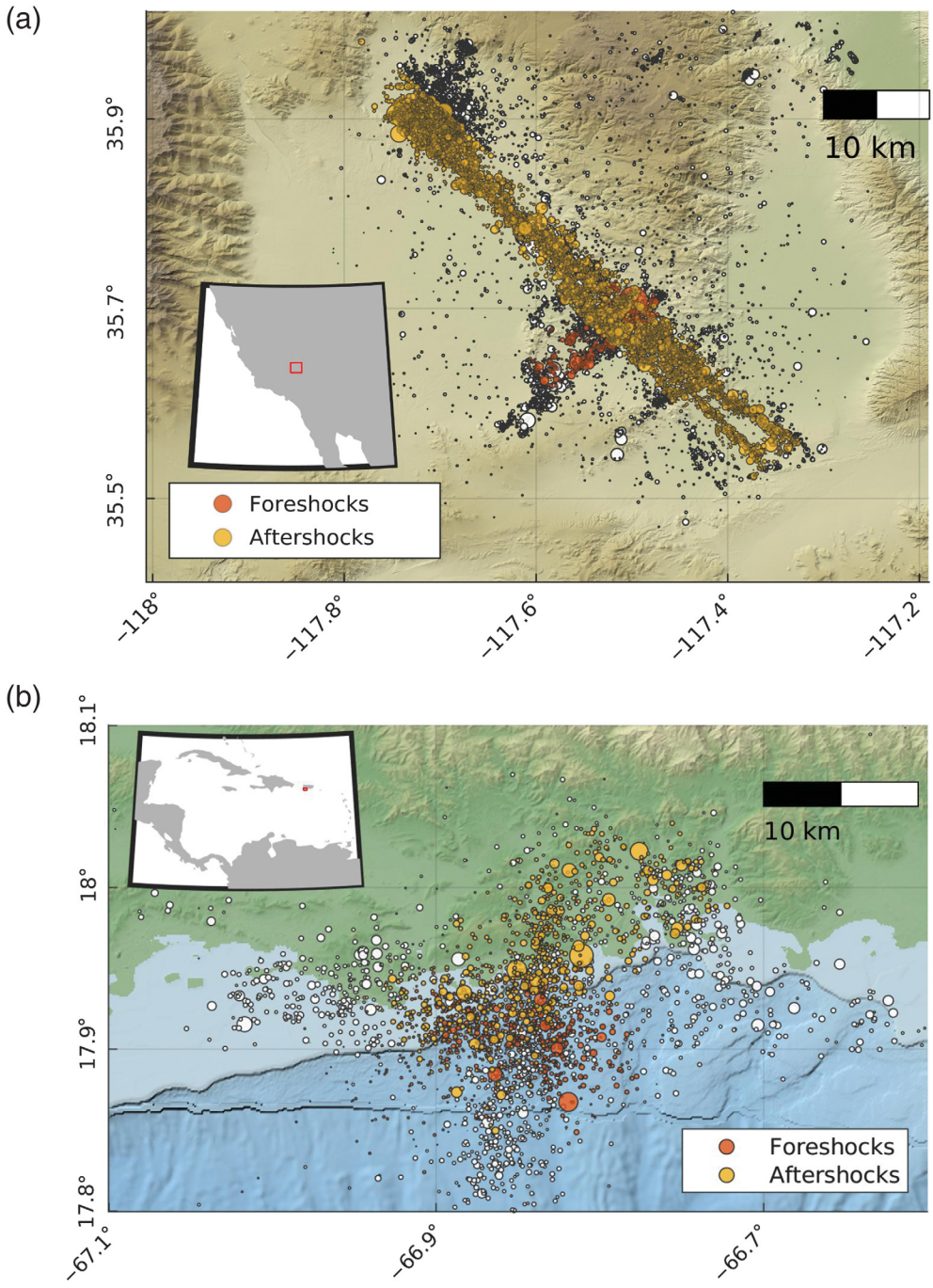

Figure 1. Overview of the seismic activity. (a) Ridgecrest earthquake activity (Shelly, 2020). (b) Earthquakes from the Puerto Rico Seismic Network. Orange and yellow events are selected for the *b*-value time series pre- and postmainshocks, respectively; note this selection is established in 3D as specified in the Appendix. Red rectangles in insets indicate study locations considered.

the Utsu (1965) correction for magnitude value round-off. Gulia and Wiemer (2019) find that a positive change in the *b*-value relative to the background value following a sizable earthquake indicates that an aftershock sequence is underway; conversely, a negative change indicates that a foreshock sequence is ongoing. Part of the approach's apparent success is attributed to the narrow space window, measurable with high-resolution catalogs, used to probe the earthquake source process (Gulia *et al.*, 2018). The authors proposed the following stop-light classification. Green: a 10% increase in the *b*-value indicates that the largest event in the region defined by the catalog has occurred and an aftershock sequence has begun; red: a 10% drop in the *b*-value indicates that a foreshock sequence is ongoing and a larger earthquake is yet to come; and orange: a change in *b*-value less than 10% is ambiguous.

Consideration of spatial and temporal *b*-values as indicators of imminent failure is not new (e.g., Molchan *et al.*, 1999). Since its first introduction as a parametric model by Gutenberg and Richter (1944), the frequency–magnitude distribution of earthquakes has been used broadly to characterize diverse seismogenic environments and probe the state of stress. Studies attribute variations in *b*-values to fault-zone heterogeneity (Mogi, 1963), stressing rate (Scholz, 1968; Wyss, 1973), variations in pore pressure (Wyss, 1973; Shaw, 1995), or thermoelastic stress relief in areas subject to high thermal gradients (Warren and Latham, 1970). The use of *b*-value as a predictive tool gained some traction in the 1970s with observations of *b*-value anomalies preceding large mainshocks (e.g., Fiedler, 1974; Smith, 1981). Similar observations in laboratory experiments suggested that *b*-value is a diagnostic of impending brittle failure (e.g., Main *et al.*, 1990). However, a low *b*-value preceding a large earthquake is, to some degree, self-fulfilling. A low *b*-value indicates a relatively high number of larger magnitude events in a sequence and thus experiencing subsequent large events should not be

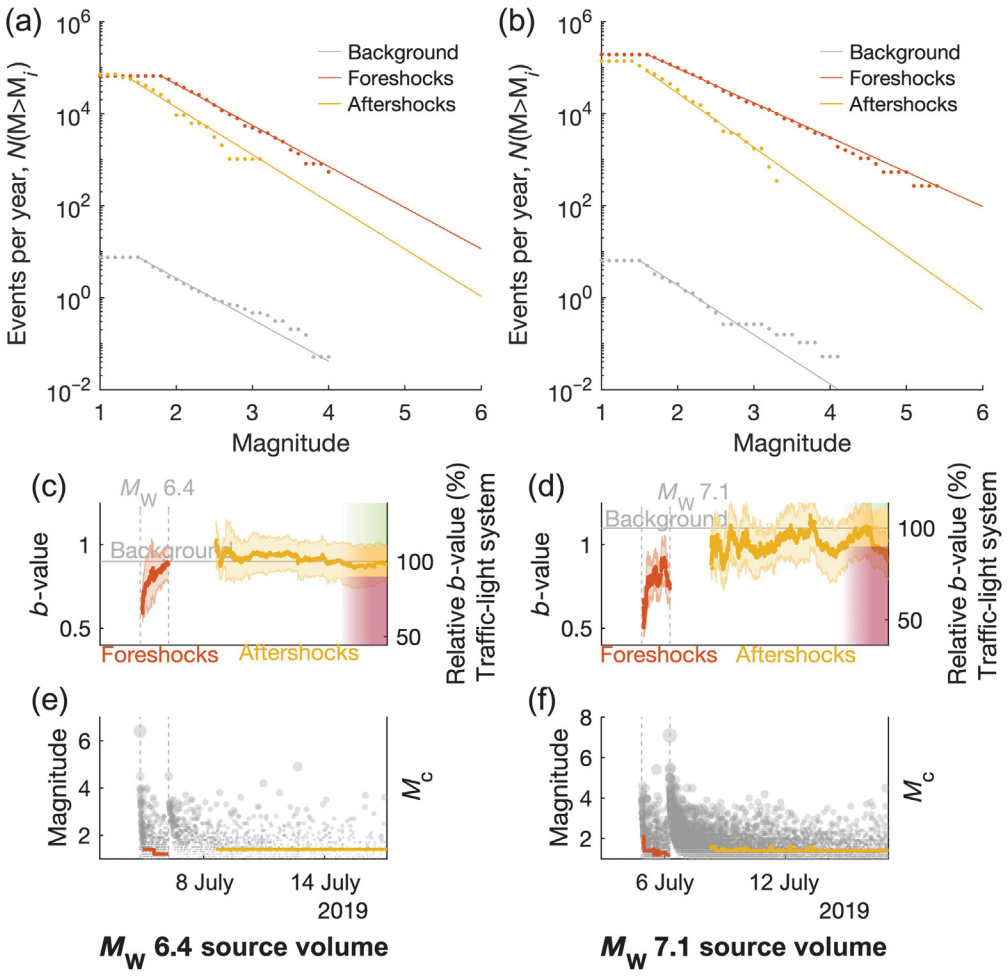

Figure 2. (a,b) Comparison of Gutenberg–Richter distributions for the background and aftershock seismicity of the Ridgecrest sequence in the M_w 6.4 foreshock and M_w 7.1 mainshock source volumes, respectively, for the time period shown in (e,f). (c,d) Time series of *b*-value estimates during the sequence with 1σ error bars for the corresponding source volumes. Dashed lines indicate the timing of the 4 July 2019 M_w 6.4 foreshock and the 5 July 2019 M_w 7.1 mainshock. The traffic-light criteria relative to the background level are indicated on the right. (e,f) Time series of event magnitudes during the sequence in the corresponding volumes. Colored curves indicated the time-varying catalog completeness, M_c, during the intervals of the foreshock and aftershock sequences used for *b*-value computation.

surprising (Helmstetter *et al.*, 2005). In the absence of high-resolution seismic catalogs with low catalog completeness, closure on this topic has been elusive.

Gulia and Wiemer (2019) suggest that earthquake sequences recorded with dense networks provide an informative window into a critical time of the earthquake cycle. Parametric earthquake forecasting models, some of which include time-varying *b*-values in a probabilistic sense, typically yield a <15% probability of a larger aftershock (e.g., Reasenberg and Jones, 1989; Hardebeck *et al.*, 2019; Shcherbakov *et al.*, 2019). The 95% success rate of Gulia and Wiemer seemingly outperforms the forecasting models by a large margin and implies that a remarkable degree of measurable determinism underlies earthquake sequences.

In predictive studies of this nature, hypotheses are inevitably developed and tested on the same data set. Confirmation bias and overfitting are a concern. Moreover, further testing in different geological environments is necessary. Recent earthquake foreshock sequences in Ridgecrest, California, and Maria Antonia, Puerto Rico, provide an opportunity to put the method, as specified, to the test. We apply the analysis to these two sequences. The details of the implementation are in the Appendix of this article.

Results

On 4 July 2019, an M_w 6.4 earthquake ruptured previously unmapped orthogonal faults near Ridgecrest (e.g., Liu *et al.*, 2019; Ross *et al.*, 2019). A very productive sequence of earthquakes followed this event (e.g., Ross *et al.*, 2019; Shelly, 2020). Two days later, an M_w 7.1 earthquake ruptured a northwest-trending fault system (Fig. 1a). This sequence was well recorded by the local network. Relocated catalogs enhanced by template matching were available promptly after the bulk of the sequence. High-resolution seismicity catalogs reveal complex faulting with multiple secondary structures of the orthogonal set on a range of scales (Fig. 1a; e.g. Ross *et al.*, 2019; Shelly, 2020).

On 28 December 2019, M_w 4.7 and, a few hours later, M_w 5.0 earthquakes marked the start of a vigorous sequence of small earthquakes just south of Maria Antonia, Puerto Rico, with over 400 recorded events in the next 10 days (Fig. 1b). On 6 January 2020, an M_w 5.8 earthquake struck, followed the next day by an M_w 6.4 event with a normal-faulting mechanism (Liu *et al.*, 2020). At present, the latter event appears to be a mainshock. In the month following the mainshock, the productivity of this sequence was remarkably high (96th percentile globally when accounting for magnitude, following Dascher-Cousineau *et al.*, 2020). The high productivity and occurrence of numerous large events before and after the mainshock suggest features

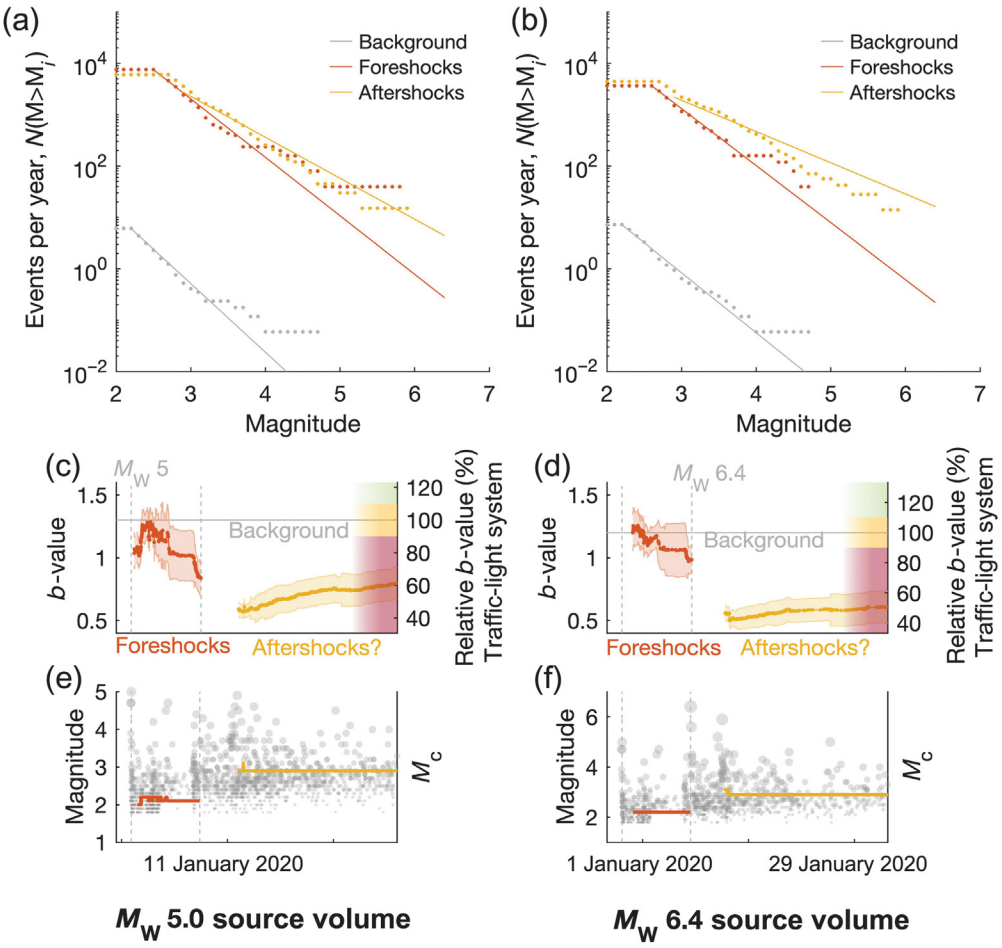

Figure 3. (a,b) Comparison of Gutenberg–Richter distributions for the background, foreshock, and aftershock seismicity of the Puerto Rico sequence in the M_w 5.0 foreshock and M_w 6.4 mainshock source volumes, respectively, for the time period shown in (e,f). (c,d) Corresponding time series of *b*-value estimates during the sequence with 1σ error bars. Dashed lines indicate the timing of the 29 December 2019 M_w 5.0 foreshock and the 7 January 2020 M_w 6.4 mainshock. The traffic-light criteria relative to the background level are indicated on the right. (e,f) Time series of event magnitudes during the sequence in the corresponding volumes. Lines indicated the time-varying catalog completeness, M_c, during the intervals of the foreshock and aftershock sequences used for *b*-value computation.

approaching those of an earthquake swarm. The largest aftershock (11 January 2020 M_w 5.9) was half a magnitude unit smaller than the mainshock, still within the typical range for largest aftershocks (Båth, 1965; Helmstetter & Sornette, 2003). The sequence occurred shoreward of the Muertos trough, a convergent zone with little recorded seismic activity (e.g., Mann *et al.*, 2005; Bruña *et al.*, 2010). Shallow hypocenters, diverse focal mechanisms, and diffuse seismicity indicate intraplate faulting on a complex network of faults (Liu *et al.*, 2020).

b-Value Time Series

We follow the procedure documented in Gulia and Wiemer (2019) by adapting their script to the new catalogs. This procedure is described in detail in the Appendix. Any deviation from the original method is indicated in the Results section.

During the Ridgecrest foreshock sequence, the *b*-value in the selected M_w 6.4 source volume is variable, rapidly increasing from 0.6 to 0.9, but lower than the estimated background level of 0.9 (measured from the nearest 250 events since 2000). A stepwise increase in *b*-value to a level generally around background in a new source volume follows the mainshock (Fig. 2). The *b*-value then continues to oscillate above and below the background for the rest of the documented period (7–16 July 2019). Gulia and Wiemer (2019) address time-varying completeness after large events by screening out affected time windows. The calibration of this blind time relies on expert judgment. If we apply a screening after the 6.4 and 7.1 of 0.05 and 2 days respectively, the stop-light procedure outlined by Gulia and Wiemer would have indicated a red warning during the foreshock sequence changing to orange during the aftershock sequence.

For the Puerto Rico earthquake sequence, the 29 December 2019 foreshock is followed by a red-warning level (Fig. 3). For the source region surrounding this event used for computing a *b*-value, we relax the nominal spatial window of 3 km from the source to 10 km to determine stable *b*-values. For this reason, the time series produced for the M_w 5.0 foreshock is not a strict test of the method proposed by Gulia and Wiemer (2019) but is nonetheless interesting to consider. In the short time window between the M_w 5.8 foreshock and the apparent mainshock, the *b*-value in the initial foreshock source volume drops further relative to background, sustaining a red warning, indicating that the activity is still a foreshock sequence. The time window between the M_w 5.8 event and the mainshock is too short to measure an independent *b*-value time series in a new box around this foreshock. For its part, the time series produced for the mainshock exactly follows the

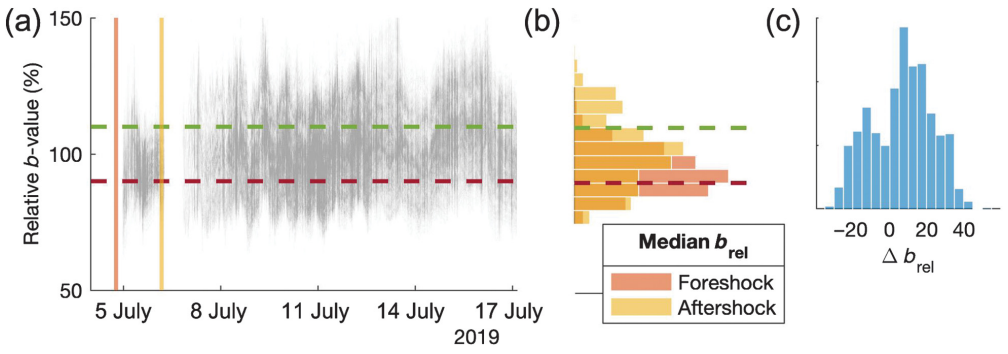

Figure 4. (a) Monte Carlo simulation of 1000 summary time series of the relative *b*-value. Each individual time series samples uniform priors for the background catalog start date (2000–2012), foreshock source volume choice (choosing one or the other of the two orthogonal planes ruptured in the foreshock), M_c maximum curvature correction (0.1–0.3), and blind times after the foreshock (0.01–0.5 days) and mainshock (0.5–5) days. Warning thresholds are indicated by the horizontal dashed lines. For all calculations, the source volume and corresponding background value are updated at the mainshock. (b) Corresponding histogram of the median relative *b*-value of the foreshock and aftershock periods. (c) Distribution of the change in the median value of the relative *b*-value after the M_w 7.1 mainshock across all the realizations.

proposed procedure. The sequence of events following the M_w 6.4 "mainshock" exhibits a further decrease in *b*-value. The postmainshock *b*-value has slowly drifted to larger values yet is still far below background level for the period we considered (Fig. 3). We estimate a high background *b*-value level ($b \sim 1.3$) for the M_w 6.4 event source volume, potentially caused by an unstable reference, and low relative *b*-values during the sequence. However, the 50% decrease in *b*-value after the M_w 6.4 event relative to the earlier activity (independent of background-level uncertainty) conflicts with the model expectations if this is a mainshock with ensuing aftershocks.

Discussion

For the Ridgecrest sequence, the procedure proposed by Gulia and Wiemer (2019) appears to characterize distinct behavior in the reference source volumes of the foreshock sequence ($b = 0.8 \pm 0.1$) relative to the aftershock sequence ($b = 1.0 \pm 0.1$). The aftershocks, however, are not distinctly above the background level. For the Puerto Rico sequence, the foreshock sequence is difficult to diagnose conclusively due to catalog irregularities and sparse background seismicity in a relatively small M_w 5.0 source volume. Although we deviate from the original method by considering a foreshock event with $M_w < 6.0$ and expanding the source volume, we do find a *b*-value drop and a red warning leading up to the mainshock, in agreement with the prediction. Events following the M_w 6.4 mainshock were distinctly vigorous and, on average, large, consistent with *b*-values far below background levels. As of 12 February 2020, there is no *b*-value increase to indicate the transition to an aftershock sequence, and the stop-light procedure predicts that a larger event is yet to come. Time will tell; however, if no larger mainshock occurs, the *b*-value procedure for identifying a foreshock sequence will fail in this instance.

Both sequences feature volatile *b*-value time series, raising an issue of real-time warning levels. A single representative *b*-value for the foreshock sequence is not a straightforward product of the method, as stated. Real-time measurements from the 400 event moving window would be highly erratic; conversely, the time window used to produce the aggregated measurements shown in Figures 2a and 3a can only be established retrospectively once the mainshock has occurred. How to robustly bridge this gap remains an open question.

The stop-light warnings are critically sensitive to (1) reliable estimation of background *b*-value in the specified source regions around the largest events, (2) time-varying catalog completeness and quality, and (3) parameterization of the *b*-value measurement. For instance, during the review of this article, we learned that the original authors of the study obtained results on Ridgecrest that deviated significantly from ours using the same catalogs and an adaptation of the published code (Gulia *et al.*, 2020). Discrepancies in the resulting time series arise from the decisions left to expert judgment that must be tuned to the individual circumstances of each earthquake. The need to pick one of two possible fault planes, when both appeared to have ruptured, further complicates the implementation.

To illustrate the importance of these factors, we performed a Monte Carlo simulation that randomly sampled a reasonable range of possibilities within the method's scope. The time series shown in Figure 4 illustrate how minor differences impact warning for the Ridgecrest sequence. For this analysis, we uniformly sampled the range of reasonable source volume (orthogonal planes ruptured in the foreshock), assumed completeness threshold correction (0.1–0.3), background catalog start date (2000–2012), and blind times following the foreshock (0.01–0.5 days) and mainshock (0.5–5 days). The variability introduced by these decisions exceeds the standard deviation of the measured *b*-values (Shi and Bolt, 1982). The relative *b*-value after the Ridgecrest mainshock generally rises after the mainshock with a modal value of a 10% increase (Fig. 4c). Yet from the set of 1000 Monte Carlo simulations, 7.4% of the time series correctly identify the foreshock and aftershock sequence and 76.7% provide neutral assessments

that do not contradict the observed outcome. The correct identifications are possible, perhaps even preferable, given careful expert judgment in the specification of parameters, but are not a representative outcome of allowable decisions.

Both sequences did not rupture plate boundary faults. Correspondingly low background seismicity causes unstable estimates of background *b*-values and, ultimately, warning levels. Should there not be enough events in the 3 km wide source volume (<250), Gulia and Wiemer (2019) measure the background *b*-values using the nearest 250 events leading up to the sequence. Background *b*-values can thus be sensitive to anomalous seismicity clusters far from the source volume. In the Ridgecrest region, for example, background activity established far from the source volume is influenced by anomalous seismicity in the Coso volcanic field; background activity considering events too far back in time is influenced by changes in the detection capabilities of the seismic network. Production of stable regionalized *b*-value maps to serve as references for temporal changes during future large event sequences is a requirement for this general approach.

During highly productive earthquake sequences, a combination of technical and logistical factors results in unstable and time-varying catalog completeness. Extraneous factors, including analyst overwhelm (person power) and damaged infrastructure, may cause *b*-values to fluctuate as an artifact of varying catalog completeness. Gulia and Wiemer (2019) partially addressed this issue by re-evaluating the catalog completeness at each windowing step and removing events in the immediate wake of larger foreshocks and mainshocks based on expert judgment. The impact of large events on catalog completeness varies with time and regional network operations. The maximum-likelihood estimation of the *b*-value is most sensitive to small events, which are likely incomplete beyond the maximum curvature threshold used to infer completeness.

The limitations outlined earlier are practical. Method development and the dedication of resources during ongoing sequences would mitigate these problems. Nonetheless, the Puerto Rico sequence highlights other potential limitations. The prediction that the sequence is a foreshock sequence is not yet fulfilled. Is this an indication that the method is not as deterministic as originally envisioned? Or is it a peculiarity of a complex tectonic environment with unusually swarmlike seismicity? How the method applies to different environments and types of earthquake sequences must still be established.

Conclusion

The procedure of Gulia and Wiemer (2019) offers the potential to recognize foreshock sequences in real time. The Ridgecrest sequence roughly conforms to expectations but is not a definitive success. The Puerto Rico sequence appears to not follow the predicted behavior but could potentially do so in the future if a larger event occurs with an ensuing *b*-value increase. We find that variable warning levels result from subtle differences in catalog production and model parameterization left to expert judgment. Future implementation of this approach will require robust decision making, well-calibrated maps of regionalized background *b*-values for a large distribution of possible source volumes, consistent and version-controlled low completeness catalogs during sequences, dense instrumentation, and systematic real-time catalog production.

Data and Resources

Figures and analysis were all produced using the MATLAB (available at www.mathworks.com/products/matlab, last accessed March 2020) version R2019b. Map figures were specifically produced using TopoToolbox and used topographic data from the Global Multi-Resolution Topography (GMRT) data synthesis and Advanced Land Observation Satellite (ALOS) Global Digital Surface Model (AW3D30) hosted on OpenTopography. Earthquake event catalogs for Ridgecrest were from the Advanced National Seismic System (ANSS) Comprehensive Earthquake Catalog (ComCat) and augmented by Shelly (2020) for events that occured during the sequence itself. Earthquake event catalogs for Puerto Rico were downloaded from the Puerto Rico Seismic Network.

Acknowledgments

The authors would like to thank the members of the University of California Santa Cruz (UCSC) seismology laboratory for providing thoughtful insight and lively debate on the topic. The authors thank an anonymous reviewer and Laura Gulia for comments on the original article. This work was funded by National Science Foundation (NSF)-Division of Earth Science (EAR) Grant 1761987 (E. E. B.) and NSF-EAR Grant 1802364 (T. L.). To the best of the authors' knowledge, no author has any conflict of interest publishing this research.

References

Aki, K. (1965). Maximum likelihood estimate of *b* in the formula $\log N = a - bM$ and its confidence limits, *Bull. Earthq. Res. Inst.* **43,** 237–239.

Båth, M. (1965). Lateral inhomogeneities in the upper mantle, *Tectonophysics* **2,** 483–514.

Bouchon, M., V. Durand, D. Marsan, H. Karabulut, and J. Schmittbuhl (2013). The long precursory phase of most large interplate earthquakes, *Nature Geosci.* **6,** no. 4, 299–302, doi: 10.1038/ngeo1770.

Brodsky, E. E., and T. Lay (2014). Recognizing foreshocks from the 1 April 2014 Chile earthquake, *Science* **344,** no. 6185, 700–702.

Bruna, J. G., A. Muñoz-Martín, U. S. Ten Brink, A. Carbó-Gorosabel, P. L. Estrada, J. Martín-Dávila, D. Córdoba-Barba, and M. C. Morollón (2010). Gravity modeling of the Muertos Trough and tectonic implications (north-eastern Caribbean), *Marine Geophys. Res.* **31,** no. 4, 263–283.

Dascher-Cousineau, K., E. E. Brodsky, T. Lay, and T. H. W. Goebel (2020). What controls variations in aftershock productivity? *J. Geophys. Res.* doi: 10.1029/2019JB018111.

Fiedler, B. G. (1974). Local *b*-values related to seismicity, *Tectonophysics* **23,** 277–282.

Gulia, L., and S. Wiemer (2019). Real-time discrimination of earthquake foreshocks and aftershocks, *Nature* **574,** 193–199, doi: 10.1038/s41586-019-1606-4.

Gulia, L., A. P. Rinaldi, T. Tormann, G. Vannucci, B. Enescu, and S. Wiemer (2018). The effect of a mainshock on the size distribution of the aftershocks, *Geophys. Res. Lett.* **45,** no. 24, 13–277.

Gulia, L., S. Wiemer, and G. Vannucci (2020). Prospective evaluation of the foreshock traffic light system in Ridgecrest and implications for aftershock hazard assessment, *Seismol. Res. Lett.* doi: 10.1785/0220190307.

Gutenberg, B., and C. F. Richter (1944). Frequency of earthquakes in California, *Bull. Seismol. Soc. Am.* **34,** 185–188.

Hardebeck, J. L., A. L. Llenos, A. J. Michael, M. T. Page, and N. Van Der Elst (2019). Updated California aftershock parameters, *Seismol. Res. Lett.* **90,** no. 1, 262–270.

Helmstetter, A., Y. Y. Kagan, and D. D. Jackson (2005). Importance of small earthquakes for stress transfers and earthquake triggering, *J. Geophys. Res.* **110,** B05508, doi: 10.1029/2004JB003286.

Helmstetter, A., and D. Sornette (2003). Båth's law derived from the Gutenberg–Richter law and from aftershock properties, *Geophys. Res. Lett.* **30,** 2069, doi: 10.1029/2003GL018186.

Helmstetter, A., D. Sornette, and J.-R. Grasso (2003). Mainshocks are aftershocks of conditional foreshocks: How do foreshock statistical properties emerge from aftershock laws, *J. Geophys. Res.* **108,** 2046, doi: 10.1029/2002JB001991.

Liu, C., T. Lay, E. E. Brodsky, K. Dascher-Cousineau, and X. Xiong (2019). Coseismic rupture process of the large 2019 Ridgecrest earthquakes from joint inversion of geodetic and seismological observations, *Geophys. Res. Lett.* **46,** 11,820–11,829, doi: 10.1029/2019GL084949.

Liu, C., T. Lay, Z. Wang, and X. Xiong (2020). Rupture process of the 7 January 2020, M_w 6.4 Puerto Rico earthquake, *Geophys. Res. Lett.* **47,** e20220GL087718, doi: 10.1029/2020GL087718.

Main, I. G., P. D. Meredith, P. R. Sammonds, and C. Jones (1990). Influence of fractal flaw distributions on rock deformation in the brittle field, *Geol. Soc. Lond. Spec. Publ.* **54,** 71–79.

Mann, P., J. C. Hippolyte, N. R. Grindlay, and L. J. Abrams (2005). Neotectonics of southern Puerto Rico and its offshore margin, in *Active Tectonics and Seismic Hazards of Puerto Rico, the Virgin Islands, and Offshore Areas*, Mann, P. (Editor), Vol. 385, The Geological Society of America, Boulder, Colorado, 173–214.

Marsan, D., A. Helmstetter, M. Bouchon, and P. Dublanchet (2014). Foreshock activity related to enhanced aftershock production, *Geophys. Res. Lett.* **41,** no. 19, 6652–6658, doi: 10.1002/2014GL061219.

Mignan, A. (2015). The debate on the prognostic value of earthquake foreshocks: A meta-analysis, *Sci. Rep.* **4,** no. 1, 4099, doi: 10.1038/srep04099.

Mogi, K. (1963). Some discussions on aftershocks, foreshocks and earthquake swarms. *Bull. Earthq. Res. Inst. Tokyo Univ.* **41,** 595–614.

Molchan, G. M., T. L. Kronrod, and A. K. Nekrasova (1999). Immediate foreshocks: Time variation of the *b*-value, *Phys. Earth Planet. In.* **111,** nos. 3/4, 229–240.

Reasenberg, P. A., and L. M. Jones (1989). Earthquake hazard after a mainshock in California, *Science* **243,** 1173–1176.

Ross, Z. E., B. Idini, Z. Jia, O. L. Stephenson, M. Zhong, X. Wang, Z. Zhan, M. Simons, E. J. Fielding, S. H. Yun, *et al.* (2019). Hierarchical interlocked orthogonal faulting in the 2019 Ridgecrest earthquake sequence, *Science* **366,** 346–351, doi: 10.1126/science.aaz0109.

Scholz, C. (1968). The frequency–magnitude relation of microfracturing in rock and its relation to earthquakes, *Bull. Seismol. Soc. Am.* **58,** 399–415.

Seif, S., J. D. Zechar, A. Mignan, S. Nandan, and S. Wiemer (2019). Foreshocks and their potential deviation from general seismicity, *Bull. Seismol. Soc. Am.* **109,** no. 1, 1–18, doi: 10.1785/0120170188.

Shaw, B. E. (1995). Frictional weakening and slip complexity in earthquake faults, *J. Geophys. Res.* **100,** 18,239–18,251.

Shcherbakov, R., J. Zhuang, G. Zöller, and Y. Ogata (2019). Forecasting the magnitude of the largest expected earthquake, *Nat. Commun.* **10,** no. 1, 1–11.

Shelly, D. R. (2020). A high-resolution seismic catalog for the initial 2019 Ridgecrest earthquake sequence: Foreshocks, aftershocks, and faulting complexity, *Seismol. Res. Lett.* **91,** no. 4, 1971–1978, doi: 10.1785/0220190309.

Shi, Y., and B. A. Bolt (1982). The standard error of the magnitude-frequency *b* value, *Bull. Seismol. Soc. Am.* **72,** no. 5, 1677–1687.

Smith, W. D. (1981). Evidence for precursory changes in the frequency–magnitude *b*-value, *Geophys. J. Roy. Astron. Soc.* **86,** 815–838.

Trugman, D. T., and Z. E. Ross (2019). Pervasive foreshock activity across southern California, *Geophys. Res. Lett.* **46,** no. 15, 8772–8781, doi: 10.1029/2019GL083725.

Utsu, T. (1965). A method for determining the value of *b* in a formula $\log n = a - bm$ showing the magnitude–frequency relation for earthquakes, *Geophys. Bull. Hokkaido Univ.* **13,** 99–103.

Warren, N. W., and G. V. Latham (1970). An experimental study of thermally induced microfracturing and its relation to volcanic seismicity, *J. Geophys. Res.* **75,** 4455–4464.

Wells, D. L., and K. J. Coppersmith (1994). New empirical relationships among magnitude, rupture length, rupture width, rupture area, and surface displacement, *Bull. Seismol. Soc. Am.* **84,** no. 4, 974–1002.

Wyss, M. (1973). Towards a physical understanding of the earthquake frequency distribution, *Geophys. J. Roy. Astron. Soc.* **31,** 341–359.

Appendix

We follow the procedure outlined by Gulia and Wiemer (2019). For the Ridgecrest sequence, we use events starting on January 2000 from the Advanced National Seismic System Comprehensive Earthquake Catalog (see Data and Resources) up until the first 4 July M_w 6.4 earthquake, after which we use the augmented catalog produced by Shelly (2020). For the Puerto Rico sequence, we use events from the Puerto Rico Seismic Network starting on January 2003. Although the sequence was offshore, the shallow seismicity was proximal enough to be well within the instrumental coverage of the local seismic network. We select the starting dates in both catalogs to maximize the number of events while ensuring generally consistent catalog practices.

The analysis is restricted to the local source regions of the large events of interest. The source region is established as follows. First, two candidate planes are obtained from the Global Centroid Moment Tensor catalog. The strike and dip of the plane that best fits the aftershock distribution is chosen. In the case of Ridgecrest, this determination is ambiguous and depends on the early time period we select to determine the source volume.

We present results for the east–west volume in Figure 2. Next, the lateral dimensions of the fault are derived from standard scaling relationships, $SRL = 10^{0.62M-2.57}$[km] (Wells and Coppersmith, 1994). Finally, the width of the source region is set to 3 km. When a new large event occurs, the source location, attitude, and lateral dimensions are updated accordingly. For the Puerto Rico sequence, these strict criteria result in too few events during the foreshock sequence. We relax these spatial criteria to a 10 km radius sphere for this specific foreshock sequence. We use a sphere because the lateral dimensions, which follow Wells and Coppersmith (1994) are less than the 10 km radius. We only deviate from the original method for this event. Our analysis of the mainshock conforms to the original method. In a preliminary screening of the catalog, all events below catalog completeness as determined by maximum curvature with a correction factor of 0.2 are removed. In addition, we remove all events within the 0.05 day window of the foreshock events in the sequence when catalog completeness is highly inhomogeneous. For mainshocks, we remove all events within two days. Pre- and postsequence events and corresponding *b*-value time series are treated separately. The time series of the presequence background level is constructed by marching forward with a 250 event window. Within this window, events are again screened for completeness. In doing so, we correct an apparent error in the published code and ensure that this second completeness screening is performed as described in the original method. The *b*-value for the group of earthquakes is estimated using maximum likelihood (equation 1) if there are more than 50 remaining events after screening. Corresponding 1σ error is established in accordance with Shi and Bolt (1982). If there are too few earthquakes to establish background, the nearest 250 events to the first event are used to measure the background *b*-value. This alternative approach is used for both Ridgecrest and Puerto Rico. Following the onset of the sequence, *b*-value estimates proceed with a 400 event window and the same completeness screening. For each event, we ensure the time series is acausal (does not include information from future events) such that a *b*-value is attributed to the time stamp of the last earthquake in the group.

Manuscript received 21 February 2020
Published online 8 July 2020